

Article

Simulation Study on the Factors Affecting the Solidification of Liquid Droplets with Different Salinity on Cold Surfaces

Zhongyi Wang, Zhiwei Deng, Yanhua Wang * and Yi Yi

College of Power and Energy Engineering, Harbin Engineering University, Harbin 150001, China

* Correspondence: wangyanhua@hrbeu.edu.cn

Abstract: Salt spray splashing on the structural surfaces of ships is a common difficulty in polar navigation. In this paper, experiments are designed to study the variation in the growth peak of pure water droplets on the surface of a hydrophobic coating with a contact angle of 90° , and the numerical simulation method is verified according to the experiment. The variation in the growth peak calculated by the numerical simulation is consistent with the experiment, and the calculation error of the freezing time obtained by numerical simulation is less than 10% of that of the experiment. The freezing processes of droplets with salinity levels of 0, 10, 20, 30, 40, and 10 μL on the surfaces of the hydrophilic, hydrophobic, and super hydrophobic plates are studied. The freezing time of the droplets is calculated, along with the effects of the wall temperature, surface contact angle, and salinity on the freezing time and freezing process of the droplets. The results show that the freezing time increased dramatically with increasing salinity. The influence of the contact angle and substrate temperature on the freezing process was also concentrated. All these results contribute to a better understanding of the icing mechanism on marine surfaces.

Keywords: saline droplets freeze; numerical modelling; sensitivity analysis; droplet growth peak



Citation: Wang, Z.; Deng, Z.; Wang, Y.; Yi, Y. Simulation Study on the Factors Affecting the Solidification of Liquid Droplets with Different Salinity on Cold Surfaces. *Appl. Sci.* **2023**, *13*, 994. <https://doi.org/10.3390/app13020994>

Received: 4 November 2022

Revised: 3 January 2023

Accepted: 4 January 2023

Published: 11 January 2023



Copyright: © 2023 by the authors. Licensee MDPI, Basel, Switzerland. This article is an open access article distributed under the terms and conditions of the Creative Commons Attribution (CC BY) license (<https://creativecommons.org/licenses/by/4.0/>).

1. Introduction

The icing phenomenon exists in many industries, such as aviation [1], electric power [2–4], energy storage [5,6], meteorology [7–9], and other fields related to people's livelihood and infrastructure construction. In some areas, the presence of ice can be harmful. As a future energy and resource base, the polar region has an increasingly prominent strategic position and will become one of the key arenas for all countries in the future. In order to ensure the normal navigation of gas turbine ships in the Arctic and Antarctic, it is necessary to study the icing phenomenon of ships in the marine environment. In the marine environment, the phenomenon of salt water freezing on the surface of ships often occurs. Various studies have shown that salinity has an obvious influence on the freezing time of droplets and it can greatly reduce the speed of the freezing peak. Currently, most of the studies on surface freezing have been concerned with the freezing phenomenon of pure water on a specific surface [10–28]. Experimental methods and numerical simulation methods are usually used to study the freezing process of droplets. Boinovich [29] investigated the freezing process of droplets on a cold superhydrophobic substrate. They observed a considerable delay in nucleation in saltwater compared to freshwater. M Strub [30] studied the behavior of droplets from the supercooled liquid phase to the liquid–solid phase and then to the solid phase on the basis of experimental studies. These three transformations are caused by various exchanges: heat transfer by conduction and convection and mass transfer by evaporation and sublimation. The phenomenon of supercooling was naturally observed in the experimental process and was considered in the modeling process. Antonini [31] investigated the effect of surface moisture on droplets impacting dry solid walls. The droplet kinematic characteristics under nine different surfaces and 12 impact velocities were analyzed with contact angles ranging from 48° to 166° . It was found that when the

Weber number was greater than 200, the surface contact angle had little influence on the spread coefficient because the inertia force was significantly greater than the capillary force. Alizadeh et al. [32] used an infrared thermal imager and high-speed camera to study the static freezing process of droplets. The test surface was a smooth silicon surface and a micro/nano silicon surface, and the test object was a 6-microliter static droplet. The influence of the temperature curve and surface contact angle on the freezing process of the droplet was studied. Chaudhary et al. [33] studied the freezing process of droplets under different wetting conditions. In their study, invasive and non-contact measurements were used to record the changes in the droplets' internal temperature during the freezing process to determine their cooling and phase transformation process. It was found that the freezing time of the droplets depended on the melting temperature and the surface moisture of the wall. A heat transfer simulation during freezing was carried out using a model based on enthalpy–porosity to understand the heat transfer in the freezing process. The droplet freezing stage was numerically analyzed and compared with the experimental results. The droplet freezing time was in good agreement with the experimental data. Sun et al. [34] used the lattice Boltzmann method (LBM) to establish a model and studied the solidification process of water droplets on a cold plate using velocity and temperature distribution functions. Using the LBM model, the solidification process is simulated in the form of temperature and solid phase changes of water droplets on a cold plate. The solid phase morphology during the solidification process is predicted. In addition, the LBM model is also used to study the frosting process preliminarily. The numerical results are in good agreement with the experimental data.

In this study, an experiment was designed to observe the freezing process of standing droplets and measure the complete freezing time, and the CLSVOF method and enthalpy porosity model were used to simulate the impact of salt droplets on the low-temperature wall. The freezing principles of the salt droplets with different concentrations in the static state and the impact state were obtained. The influences of the surface contact angle, wall temperature, and impact velocity on the spreading radius, droplet temperature field, velocity field, pressure field, and wall heat flux after the droplet impacted the low-temperature wall were analyzed.

2. Description of Standing Liquid Drop Test Method

The droplet freezing experiments were carried out in a Cryogenic closed laboratory with refrigeration function at Harbin Engineering University, as shown in Figure 1. The diagram of the test-bed system built at Harbin Engineering University in this study is also shown in Figure 2.

During the experiment, the closed laboratory was cooled by air conditioning to stabilize the room temperature at 16 °C. Temperature and humidity sensors were used to measure the temperature and humidity inside the test section. The copper plate was fixed on the test bench. The upper side of the copper plate was coated with hydrophobic material, and the lower side was coated with silicon grease to facilitate heat conduction. The semiconductor-cooling device and the water-cooling device were mounted on the lifting platform, and the surface of the semiconductor-cooling device was coated with a silicone coating. In the experiment, the circulating water tank and the fan radiator were always kept working to achieve the best cooling effect of the semiconductor cooling sheet. The syringe was connected to the capillary through a silica gel tube, and the droplet separated from the capillary after contacting the hydrophobic coating surface and remained on the coating surface. At that time, the initial contour shape and size parameters of the droplet could be measured by the ruler.

The camera shot at a frame rate of 100 per second, which meets the requirements of capturing the transient freezing behaviors of droplets. In the post-processing process of experimental data, video post-processing software was used to doubly calibrate the experimental process. First, the shape of the droplet in the initial state was captured, as shown in Figure 3, where the red line indicates the real contour of the droplet, below the

enclosed red area in the image is the local reflection of the droplet on the surface of the experimental metal plate. To measure the size of the actual droplet in the experiment, a ruler was installed at the bottom plate for reference in shooting and recording, and then a two-dimensional electronic ruler covering the droplet contour was established using the image post-processing method. The specific coordinates of the droplet contour were obtained from the two-dimensional electronic coordinate ruler by the point tracing method. Since the droplet itself was stable and had certain symmetry after contacting the wall, only the left droplet contour line was selected to record, and the geometric model of the droplet was established based on the axial symmetry. A temperature visualization module was provided on the surface of the semiconductor cooling sheet. After setting up the target temperature and cooling to reach it, the lifting platform was adjusted for the silicon grease on the upper surface of the semiconductor cooling sheet to make contact with the silicon grease on the lower surface of the copper sheet, hence cooling the liquid droplets on the copper sheet and the coating. The temperature collector collected the temperature of the four points of the copper plate at all times and obtained the average temperature of the whole copper plate by programming. The freezing process was recorded by the camera under light source illumination.

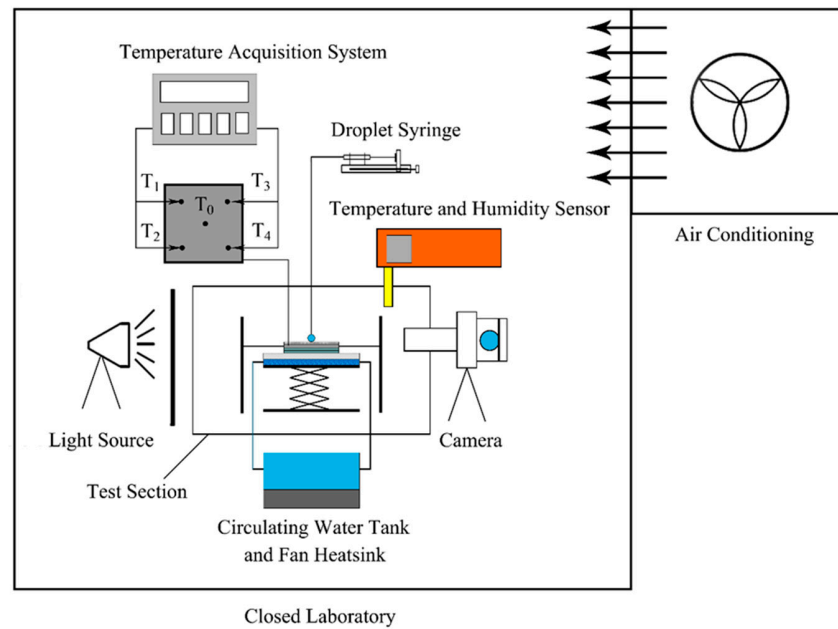


Figure 1. Schematic diagram of the experimental loop.

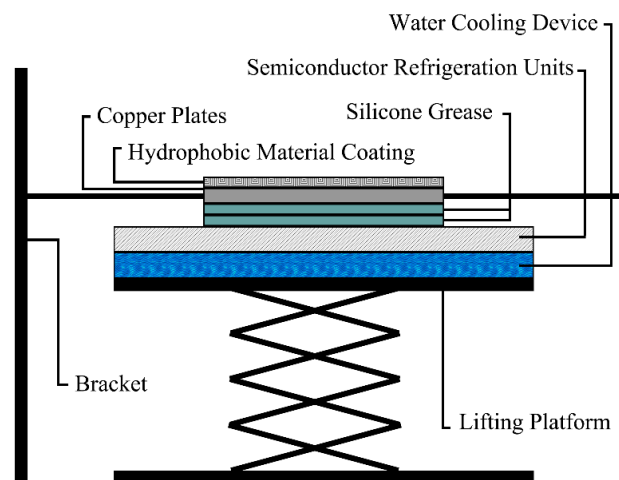


Figure 2. Testing step details.

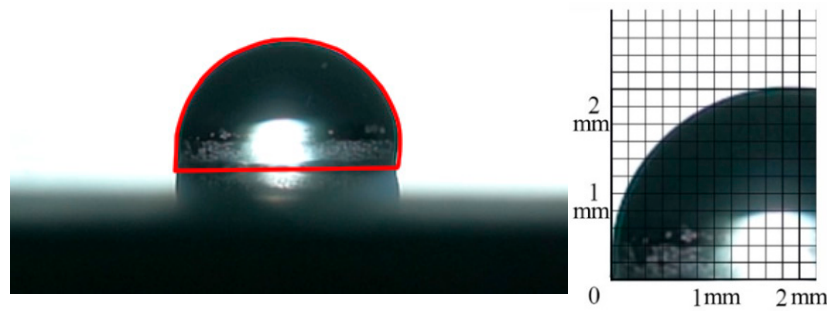


Figure 3. Outline of the initial state of the droplet.

3. Numerical Method

3.1. Geometry of a Sessile Drop

Three different cases in which the droplets rested on a flat, dry surface are shown in Figure 4. The droplets were set to the liquid phase. Ideally, the shape of a stationary droplet on a flat surface is determined by the surface tension of the droplet γ , the adhesion coefficient of the liquid–solid surface δ , the volume of the droplet V , and the contact angle of the surface θ .

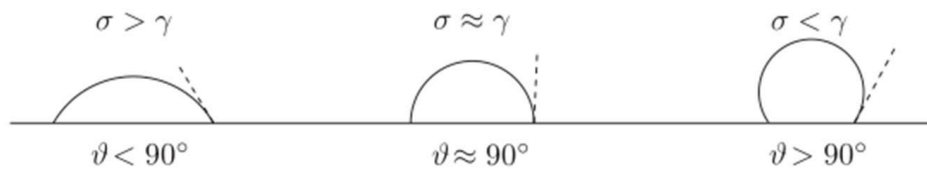


Figure 4. The shapes of droplets in three different cases.

The solution to the shape of a droplet at rest on a plane is a conicity derived from the Young–Laplace equation.

The expression of the equation is as follows:

$$\cos \theta = \frac{\sigma}{\gamma} - 1 \tag{1}$$

Each point on the surface of the droplet can be obtained in the following form of the Young–Laplace equation:

$$\gamma \left(\frac{1}{R_1} + \frac{1}{R_2} \right) = \Delta p \tag{2}$$

Δp indicates the pressure difference between the inside and outside of the droplet. R_1 and R_2 are the two main radii of the curvature of the surface at that point.

The Young–Laplace equation is a partial differential equation in which different boundary conditions determine the shape of the droplet. The final shape of the water droplet is the result of the balance of surface tension and gravity.

At the origin coordinates, the equation in Equation (3) is satisfied.

$$x(0) = z(0) = \alpha(0) = V(0) = A(0) = 0 \tag{3}$$

The governing equation for droplets standing on a plate is as follows:

$$\begin{cases} \frac{dx}{ds} = \cos \alpha \\ \frac{dz}{ds} = \sin \alpha \\ \frac{d\alpha}{ds} = 2b + cz - \frac{\sin \alpha}{x} \\ \frac{dV}{ds} = \pi x^2 \sin \alpha \\ \frac{dA}{ds} = 2\pi x \end{cases} \quad (4)$$

In Equation (3), b is the curvature of the curve at the initial point, which can be used as a target parameter, c is the curvature of the curve at the point (x_i, z_i) , s is the contour curve of the droplet, α is the angle between the tangent at the point (x_i, z_i) on s and the x -axis, V is the volume of the droplet, and A represents the cross-sectional area of the droplet.

When the value of s is equal to 0, the form of the third equation in the formula needs to be changed to Equation (4).

$$\frac{d\alpha}{ds} = b \quad (5)$$

According to this formula, using the volume of the water droplet and the contact angle of the wall surface in the initial stage, the contour of the water droplet can be calculated at the known gravitational acceleration, the surface tension of the droplet, and the droplet density. The initial conditions for the numerical simulation of static droplet freezing in this study were the droplet shapes calculated by this equation.

In this paper, the time from the appearance of the growth peak at the bottom of the droplet to the time when the growth peak reaches the top of the droplet is defined as the complete freezing time T_t . The accuracy of the experiment was tested by comparing the heights of the growth peaks at different times. The complete freezing time T_t of the droplet was used to measure the influence of different factors on the freezing rate.

A physical model, as shown in Figure 5, was established based on the water droplet profile calculated by the Young–Laplace equation. Figure 6 shows the location and boundary conditions of the droplets in the computational domain on the left and the grid on the right. The left side is the rotational symmetry axis, the right and upper sides are the pressure outlet, and the lower side is the wall surface. Different cold surfaces can be obtained by setting the wall surface temperature, and the ambient temperature can be set according to the needs of the study. Water droplets and air are modeled separately, and both use structured grids. In this study, the process of the static freezing of droplets did not consider the change of shape, and there was an energy exchange between water droplets and air but no exchange of matter, so the surface of the water droplet was set as a solid wall.

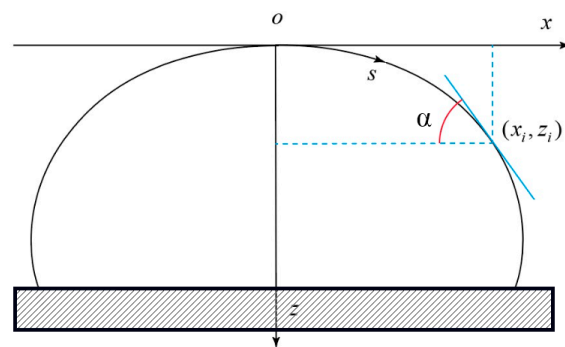


Figure 5. Calculation method of the initial state profile of the droplet.

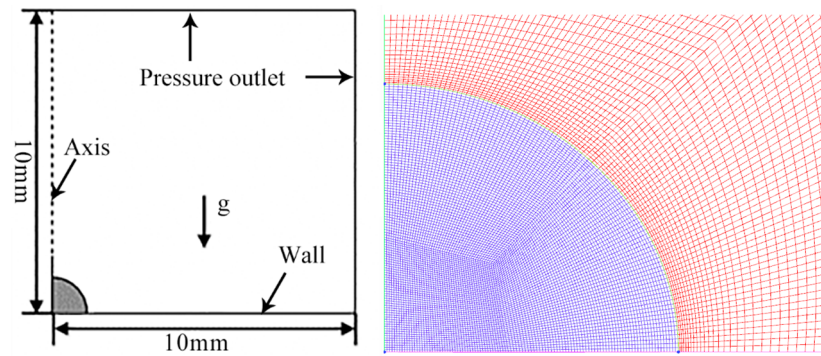


Figure 6. Physical model and mesh of static icing simulation of water droplets.

In the simulation process, the specific heat capacity, thermal conductivity, latent heat of solidification, etc., were set as a function of temperature, and when the temperature was higher than the liquefaction temperature T_{liquid} , the physical properties parameters of the liquid state were used. When the temperature was lower than T_{solid} , the physical properties of solid ice were used. The physical properties of the air did not change with the temperature change.

The main difference between pure water droplets and saline droplets in the calculation model is the difference in thermal conductivity. The thermal conductivity of pure water is, on average, $0.54 \text{ W}/(\text{m}^2 \cdot \text{K})$. The thermal conductivity of seawater is lower than that of freshwater, and the thermal conductivity becomes higher as the temperature increases. The amplitude of the reduction of seawater thermal conductivity is small compared to the specific heat ratio, and the thermal conductivity of seawater with a total salt content of 34.5‰ at $20 \text{ }^\circ\text{C}$ is reduced by about 3.6%. Seawater is less viscous than freshwater and has less surface tension than freshwater. The thermal conductivity of pure ice is $2.2186 \text{ W}/(\text{m}^2 \cdot \text{K})$, and the thermal conductivity of sea ice is formulated as follows:

$$\lambda = \lambda_0 + \beta \cdot S / (T_{sea} - 273) \tag{6}$$

where λ_0 is the thermal conductivity of pure ice, β is the scale coefficient (the value is $0.13 \text{ W}/(\text{m}^2 \cdot \text{kg})$), T_{sea} is the sea ice temperature, and S is the sea ice salinity.

The freezing point of pure water is $0 \text{ }^\circ\text{C}$, and the freezing point of seawater is different from that of freshwater, depending on how much salt it contains. Therefore, the relationship between the temperature satisfaction and salinity of the seawater freezing point in setting the seawater conforms to the following formula:

$$T_{freezing} = -0.0137 - 0.05199S - 0.00007225S^2 - 0.000758Z \tag{7}$$

where $T_{freezing}$ is the freezing temperature, S is the salinity of the sea, and Z is the depth from the sea surface.

The specific heat of pure ice is $2.0934 \text{ kJ}/(\text{kg} \cdot \text{K})$, which changes very little with the temperature. However, the specific heat of sea ice varies with temperature and salinity, and the range of change is much larger than that of pure ice. The formula for the specific heat capacity of sea ice is as follows:

$$C_p = 0.505 + 0.0018T_{sea} - 0.0008S + 0.00002S \cdot T_{sea} + 4.3115(S/T_{sea}^2) \tag{8}$$

where C_p is the specific heat capacity, $T_{surface}$ is the sea ice temperature, and S is the sea ice salinity.

The heat of freezing and heat of melting are relative terms that are quantitatively equivalent and refer to the amount of heat released or absorbed per unit weight of a liquid or solid when it freezes or melts. The heat of freezing (heat of melting) of seawater is $3.35 \times 10^5 \text{ J}/\text{kg}$. The latent heat of freezing of sea ice is also related to salinity. The latent heat formula of sea ice is as follows:

$$L = -1992S^4 + 6274.1S^3 - 6738S^2 + 2606.6S - 14.287 \tag{9}$$

where L is the latent heat, and S is the sea ice salinity.

3.2. Gas–Liquid Multiphase Model

Given incompressible and laminar flow, the governing equations of continuity and momentum are as below:

$$\nabla \times \vec{u} = 0 \tag{10}$$

$$\frac{\partial}{\partial t}[\vec{u}] + \nabla[\vec{u}\vec{u}] = -\frac{1}{\rho(\varphi)}\nabla p + \frac{1}{\rho(\varphi)}\nabla \times \vec{\tau} + \vec{g} - \vec{F}_{sf} + S_y \tag{11}$$

where \vec{u} is the velocity vector, φ is the level-set function, ρ is the density, $\vec{\tau}$ is the stress tensor, \vec{F}_{sf} is the force arising from surface tension effects, and S_y is the additional sink term induced by the solidification model.

The coupled level-set and VOF (CLSVOF) model was specifically designed for two-phase flows, a popular interface-tracking method (Sussman and Puckett, 2000). It can precisely capture the gas–liquid interface and be characterized by good conservation properties. The interface was captured and tracked by the level-set function φ , defined as a signed distance from the interface. Then, the continuity equation becomes:

$$\frac{\partial \varphi}{\partial t} + \nabla \cdot (\vec{u}\varphi) = 0 \tag{12}$$

The \vec{F}_{sf} in Equation (5) specifically represents capillary forces and is written as:

$$\vec{F}_{sf} = \sigma\kappa\delta(\varphi)\vec{n} \tag{13}$$

where σ is the liquid-phase surface tension, and κ and \vec{n} are the local mean interface curvature and local interface normal, respectively. The viscosity, density, specific heat, and thermal conductivity were reconstructed as:

$$\gamma(\varphi) = \gamma_g + (\gamma_l - \gamma_g)\varphi \tag{14}$$

The subscripts l and g represent the liquid and gas phases, respectively. A detailed description can be found in our previous studies (Liu et al., 2021 [35]; Liu et al. 2020 [36]).

3.3. Solidification Model

The solidification and melting methods based on the enthalpy–porosity formulation were used to describe the freezing of a seawater droplet. A quantity named liquid fraction β was used to track the evolution of the liquid–solid interface, which indicates the fraction in liquid form. The liquid fraction is defined as:

$$\begin{cases} \beta = 0 & (T < T_{solid}) \\ \beta = 1 & (T > T_{liquid}) \\ \beta = \frac{T - T_{solid}}{T_{liquid} - T_{solid}} & (T_{liquid} < T < T_{solid}) \end{cases} \tag{15}$$

When a liquid phase has fully solidified, the liquid fraction becomes zero; hence, the velocities drop to zero. A mush zone defined as a liquid–solid coexistence region was modeled and treated as a porous zone, where the porosity was equal to the liquid fraction,

and its value was between 0 and 1. The effect due to the reduced porosity in the mushy area was incorporated in the momentum equation sink term S_y , expressed as:

$$S_y = \frac{(1 - \beta)^2}{(\beta^3 + \epsilon)} A_{mush} \vec{u} \tag{16}$$

where ϵ is a small number (0.001) introduced to prevent division to zero. A_{mush} is the mushy zone constant, which reveals the degree of difficulty of the liquid solidification process. It was set as 108, based on Zheng et al. (Zheng et al., 2014 [37])

For the enthalpy–porosity technique, the energy equation is expressed as follows:

$$\frac{\partial}{\partial t} [\rho H] + \nabla \cdot [\rho \vec{u} H] = \nabla \cdot (\lambda \cdot \nabla T) + S_h \tag{17}$$

where λ is the thermal conductivity and H is the total enthalpy per control volume. H is computed as the sum of the sensible enthalpy h and the latent heat ΔH , expressed as:

$$H = h + \Delta H \tag{18}$$

where h is defined as $h = h_{ref} + \int_{T_{ref}}^T c_p dT$, h_{ref} is the sensible enthalpy at the reference temperature T_{ref} , and c_p is the specific heat at constant pressure. The latent heat ΔH is defined as $\beta \times L$, where L is the latent heat of the material.

The volume of all the droplets in this study was 10 μL . When using the solidification/melting model, there are two important parameters. One is the mushy zone parameter, which affects the phase transition rate and the accuracy of the calculation during the freezing process. Another important parameter is $\Delta T = T_{liquid} - T_{solid}$, which is the difference between the liquid temperature and the solid temperature, which affects the stability and the thickness of the phase interface during icing calculations. Therefore, it is very important to choose appropriate parameters for a simulation of the droplet freezing process. This study used the test value as a reference for verification; the final A_{mesh} value was B , and ΔT was 0.5 $^\circ\text{C}$.

In the method of verifying the numerical simulation calculation, according to the experimental measurements, the bottom diameter of the droplet at $-15\text{ }^\circ\text{C}$ was 4.4 mm, and the bottom diameter of the droplet at $-5\text{ }^\circ\text{C}$ was also 4.4 mm. The droplet contour model for the numerical simulation was established by pushing back the contour parameters of the droplet by the Young–Laplace equation. The complete freezing times of the droplets at $-15\text{ }^\circ\text{C}$ and $-5\text{ }^\circ\text{C}$ in the experiment are shown in Table 1 below.

Table 1. Comparison of complete freezing times.

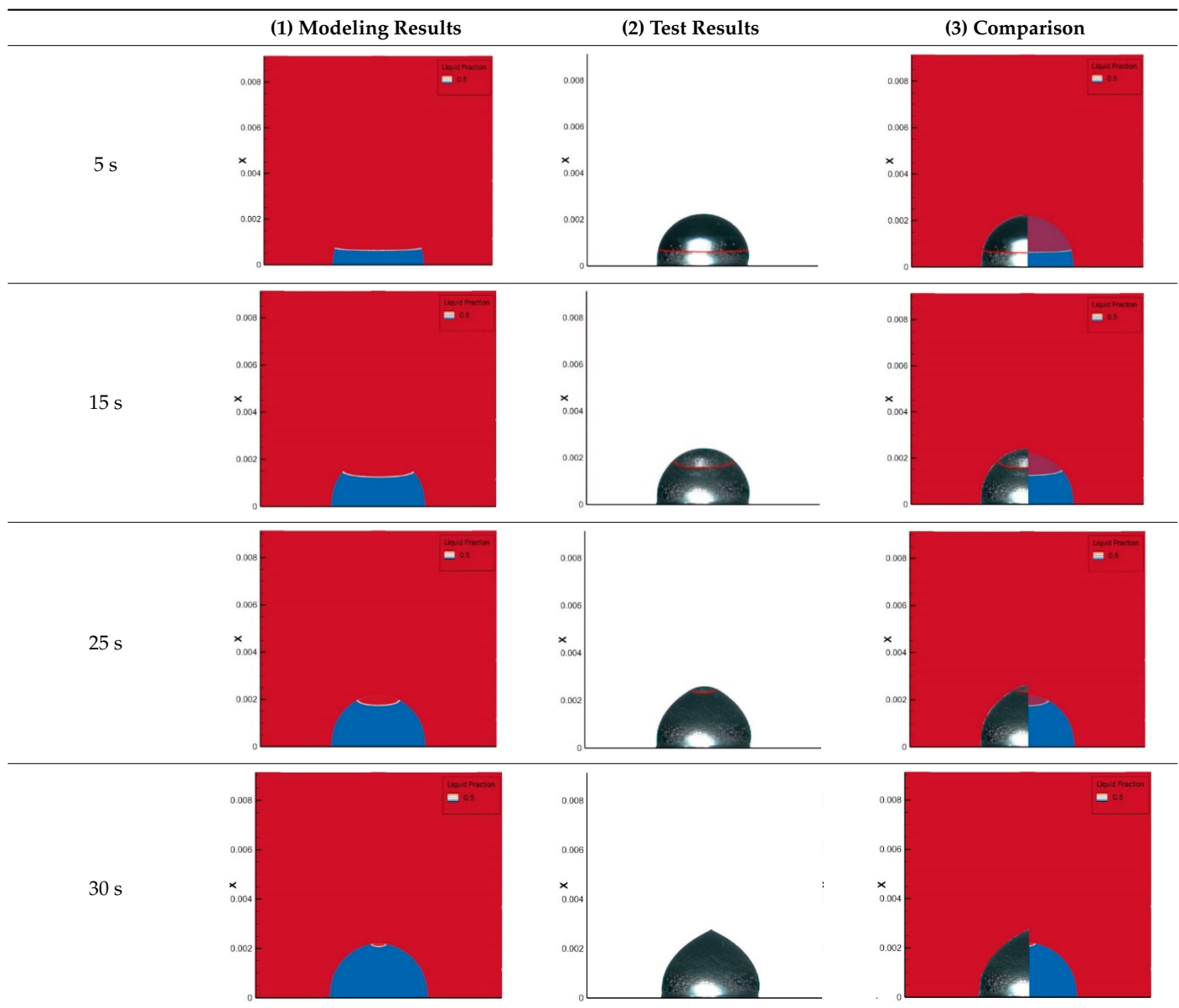
| | Test | Numerical Simulation | Relative Error |
|-----------------------------|--------|----------------------|----------------|
| $-5\text{ }^\circ\text{C}$ | 30.0 s | 31.8 s | 6% |
| $-15\text{ }^\circ\text{C}$ | 50.0 s | 52.0 s | 4% |

The solidification time of the droplets was 31.8 s, the solidification time of the droplets in the test was 30 s, and the error was less than 10%. When the wall temperature was $-5\text{ }^\circ\text{C}$, the droplet solidification time in the simulation process was 52 s, and the solidification time of the droplets in the test was 50 s. The error was less than 10%. To compare the freezing process of the simulation and the test at $-15\text{ }^\circ\text{C}$, the growth peak changes of the test and the numerical simulation are shown in the following figure, and the change process of the $-5\text{ }^\circ\text{C}$ droplet growth peak was similar to that omitted here.

Table 2 shows the comparison of numerical simulations and experiments with respect to the droplet freezing process. During the first 5s of icing, the location of the growth peak recorded in the experiment and the simulation almost exactly coincided, and the shape of the water droplets was almost unchanged. After fifteen seconds, the difference between the

simulation and the test began to appear. The position of the growth peak recorded in the experiment was slightly higher than the simulation, the shape of the droplet was slightly expanded compared to the initial state, and the distance between the growth peak of the test droplet and the growth peak of the simulated droplet could be analyzed, which was due to the volume change caused by the change in the density of the droplet when the droplet changed. In the subsequent freezing process, the difference between the position of the experimental growth peak and the simulated droplet gradually enlarged, mainly due to the difference in volume caused by the change in the density of the droplets during the experiment. Compared to the complete freezing time error of less than 10%, the simulation method is considered feasible.

Table 2. Droplet growth peak at different times.



The main variables involved in the calculation in this step are the wall contact angle θ , the temperature of the cold wall surface T_w , and the salinity of the droplet S . This step was a simulation of the static freezing process of droplets at different wall contact angles, with a hydrophilic wall contact angle of 76° , a hydrophobic wall contact angle of 110° , and a superhydrophobic wall contact angle of 150° . The cold wall temperature was set to -5°C ,

$-10\text{ }^{\circ}\text{C}$, and $-15\text{ }^{\circ}\text{C}$. The droplets were pure water droplets, $S = 10$ saline droplets, $S = 20$ saline droplets, $S = 30$ saline droplets, and $S = 40$ saline droplets. The droplet volumes were all $10\text{ }\mu\text{L}$. Table 3 contains the settings of the relevant parameters.

Table 3. Relevant parameters.

| θ | 76° | | 110° | | 150° | |
|----------|------------------------------|----|-------------------------------|----|-------------------------------|--|
| T_w | $-5\text{ }^{\circ}\text{C}$ | | $-10\text{ }^{\circ}\text{C}$ | | $-15\text{ }^{\circ}\text{C}$ | |
| S | 0 | 10 | 20 | 30 | 40 | |

4. Results and Discussion

Figure 7 shows the temperature field changes and growth peak changes during the freezing process of the liquid droplets resting on the $-5\text{ }^{\circ}\text{C}$ plate surface with different contact angles, indicating that the ice peak surface was below the temperature cloud diagram. The red is the fluid region, and the blue is the solid region. The temperature of the droplet in contact with the wall gradually decreased, and the low-temperature region spread from the bottom of the droplet to the top of the droplet as the phase change solidification process progressed. The air temperature around the droplet also gradually decreased, and heat exchange occurred with the droplet. At the beginning, the temperature of the upper of the droplet is almost constant, and the temperature of the lower part of the freezing point droplet drops rapidly, with obvious temperature difference. This is because the upper part of the droplet is not in direct contact with the cold wall. The droplet then gradually cools, approaching the freezing point. In the middle stage of the droplet freezing, the internal temperature of the droplet was close to the freezing temperature, and the temperature changes gradually slowed down. As the freezing process progressed, the temperature gradually decreased. After the droplet was completely frozen, the temperature of the droplet slowly dropped to the wall temperature. After the droplet was frozen, the temperature dropped rapidly to the wall temperature due to the small specific heat capacity and high thermal conductivity of the ice.

By comparing the temperature distribution of different contact angles, it can be seen that the contact areas between the droplets and the cold wall were quite different. On the hydrophilic wall, the contact area of the droplets and the cold surface was large; on the hydrophobic surface, the contact area of the droplets and the cold surface was small; on the superhydrophobic surface, the contact area of the droplets and the cold surface was the smallest. These results show that there was heat exchange between the droplet and the air and the cold surface. Compared to the heat exchange between the droplet and the cold surface, the heat exchange between the droplet and the air was of small magnitude. Therefore, the larger the contact area between the droplet and the wall, the greater the heat transfer between the droplet and the wall, and the faster the temperature reduction process of the droplet. Therefore, the temperature drop process of the droplet on the wall with a small contact angle was significantly faster than that of the droplet on the wall with a large contact angle.

The static phase transition solidification process of the droplet on the solid wall was also developed from the bottom of the droplet to the upper part of the droplet. The solidification time had a large relationship with the contact angle of the wall surface. It takes less time for droplets of the same volume to freeze completely on the hydrophilic wall. In comparing the growth of the droplet ice front at different contact angles, Due to the difference in the contact angle of the wall, the growth of the droplet ice front surface is quite different. On the wall surface with a small contact angle, the growth of the droplet ice front was relatively rapid, the growth of the droplet ice front was slower on the hydrophobic wall, and the growth of the droplet ice front was the slowest on the superhydrophobic wall. This is because the contact area between the droplet and the wall surface was quite different among surfaces with different contact angles. The contact area mainly affected the heat transfer process between the droplet and the wall. When the contact area was

larger, the main heat exchange between the droplet and the outside was the heat exchange between the droplet and the wall. When the contact area between the droplet and the wall was larger, the more heat transfer of the droplet and the contact area of the hydrophilic wall surface was the largest, the hydrophobic area was small, and the superhydrophobic area was the smallest. Looking at the droplets with different wall contact angles, the droplet height of the hydrophilic wall surface was the smallest, and the droplet height of the superhydrophobic wall surface was the largest. Hence, the heat transfer process of the superhydrophobic wall surface was longer, the ice front surface growth process was longer, and the freezing time was longer.

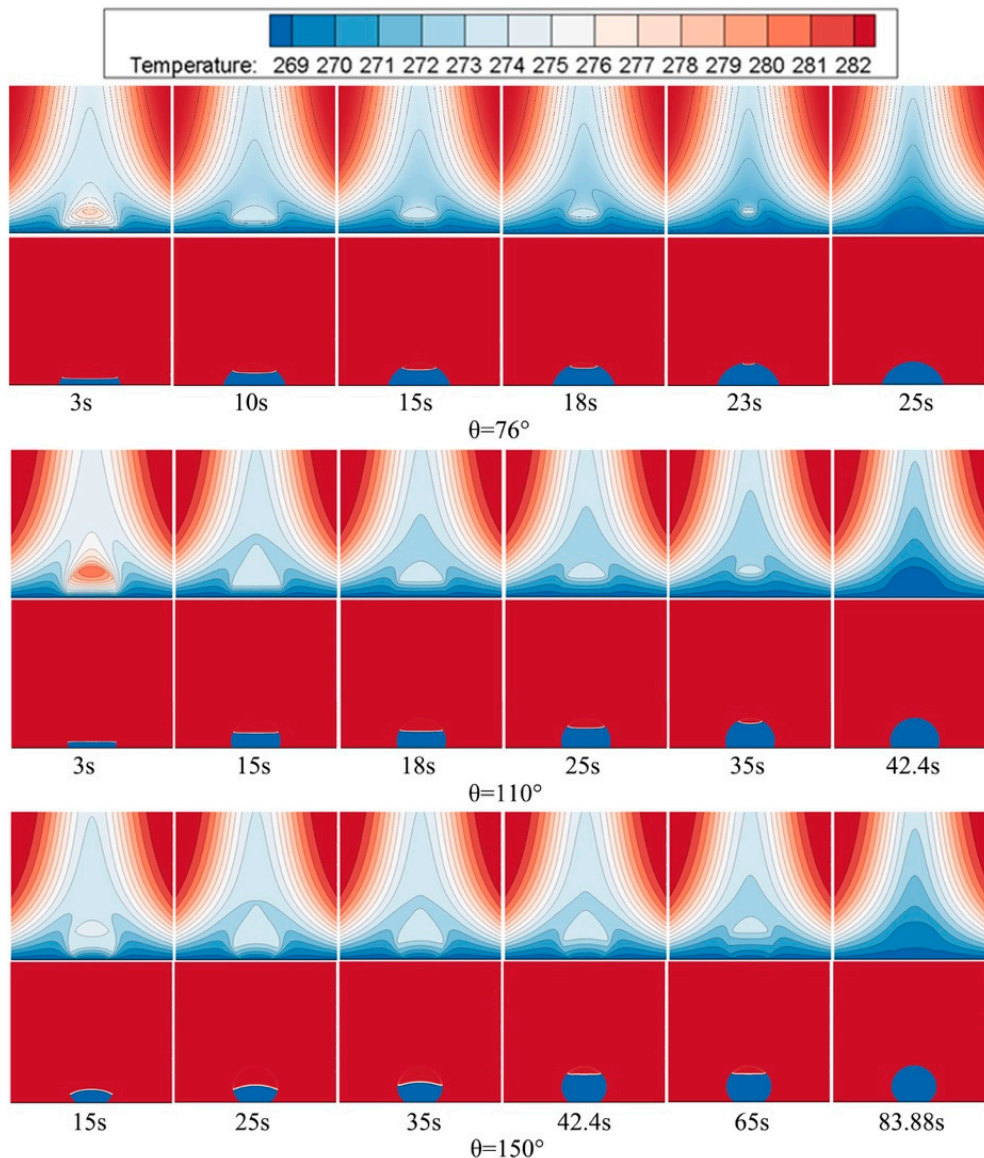


Figure 7. Temperature field distribution and growth peak change of droplet freezing on the wall at -5°C at different contact angles.

Figure 8 shows the complete freezing time T_f of the droplet under different contact angles θ , different wall temperatures T_w , and different salinity levels S . An analysis and summary of the numerical simulation results were carried out.

For the same volume of droplets, the complete freezing time increased with the increase in the contact angle, and the freezing time of the hydrophobic wall increased by about 70% compared to the hydrophilic wall. The freezing time of the superhydrophobic wall increased by about 100% compared to the hydrophobic wall. Changing the wall

characteristics and increasing the wall contact angle can effectively prevent or delay the occurrence of icing.

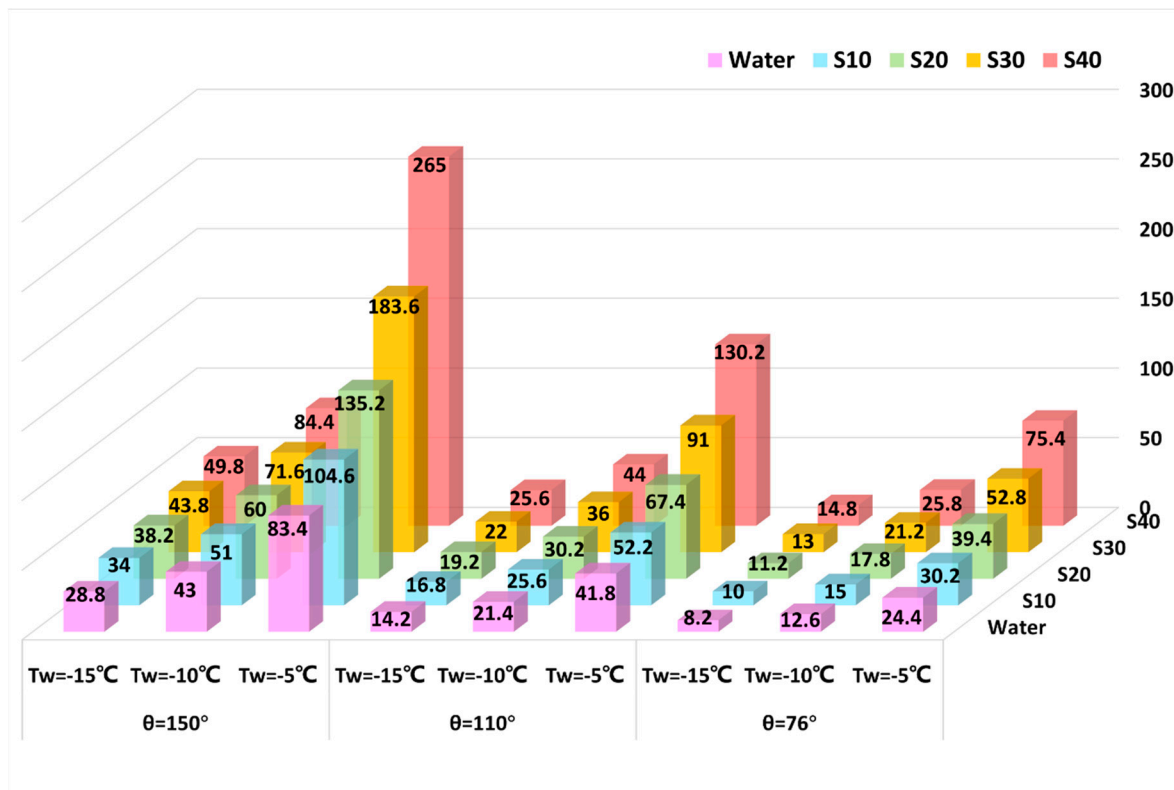


Figure 8. Complete freezing time.

The freezing time of the droplets varied with the changes in the wall temperature. The lower the wall temperature, the faster the freezing process of the droplet. The wall temperature dropped from $-5\text{ }^{\circ}\text{C}$ to $-10\text{ }^{\circ}\text{C}$, and the icing time decreased by about 50–70% for the droplets with different saline concentrations and wall contact angles. The wall temperature dropped from $-10\text{ }^{\circ}\text{C}$ to $-15\text{ }^{\circ}\text{C}$, and the icing time decreased by about 30–40%. For salt-containing droplets, the increase in the droplet salinity decreased the droplet solidification temperature, so unlike changing the contact angle, changing the wall temperature had slightly different effects on the droplets with different salinities. Increasing the wall temperature can effectively prevent or delay the occurrence of icing.

With different wall contact angles and different wall temperatures, the freezing times of the droplets changed with the changes in the droplet salinity, and the higher the droplet salinity, the longer the freezing process of the droplets. At a wall temperature of $-5\text{ }^{\circ}\text{C}$, the freezing time increased by about 25% from pure water droplets to $S = 10$ at three contact angles. From the $S = 10$ saline droplets to the $S = 20$ saline droplets, the freezing time increased by about 30%. From the saline droplets of $S = 20$ to the saline droplets of $S = 30$, the freezing time increased by about 35%. From the saline droplets of $S = 30$ to the saline droplets of $S = 40$, the freezing time increased by about 45%. At a wall temperature of $-10\text{ }^{\circ}\text{C}$, for every 10% increase in salinity at the three contact angles, the freezing time increased by about 20%. At a wall temperature of $-15\text{ }^{\circ}\text{C}$, for every 10% increase in salinity at the three contact angles, the freezing time increased by about 15%.

When the wall temperature was higher, the increase in salinity was more obvious because the increase in salinity reduced the freezing point of the droplets. When the wall temperature was $-5\text{ }^{\circ}\text{C}$, the difference between the freezing point of the pure water droplet and the wall temperature was $5\text{ }^{\circ}\text{C}$, and the difference between the freezing point and the wall temperature of the $S = 40$ saline droplets was $2.68\text{ }^{\circ}\text{C}$. When the wall temperature

was $-15\text{ }^{\circ}\text{C}$, the difference between the freezing point of the pure water droplet and the wall temperature was $15\text{ }^{\circ}\text{C}$, and the difference between the freezing point and the wall temperature of the $S = 40$ saline droplet was $12.68\text{ }^{\circ}\text{C}$. When the wall temperature decreased, the gap in the freezing point caused by the increase in salinity was smaller, so the influence of salinity became smaller. Therefore, when the wall temperature was $-5\text{ }^{\circ}\text{C}$, with the increase in salinity, the solidification time increased more and more. When the wall temperature was $-15\text{ }^{\circ}\text{C}$, with the increase in salinity, the increase in the solidification time changed less.

The method of judging the sensitivity of the influence of uncertainties on the indicator was to calculate the sensitivity factor E , as follows.

$$|E| = |(\Delta A/A_0)/(\Delta B/B_0)| \quad (19)$$

where $\Delta A/A_0$ is the rate of change of the evaluation index, $\Delta B/B_0$ is the rate of change of the uncertainty factor. The larger $|E|$ is, the more obvious the impact of the change in the evaluation index on the uncertainty factor is; the smaller $|E|$ is, the less obvious the impact is.

Figure 9 shows the results of the sensitivity effect of T_t at different contact angles θ , different wall temperatures, and different salinity values S on the sensitivity of T_t . According to the calculation of the sensitivity analysis, the sensitivity coefficient $|E|$ was calculated, and the complete freezing time at a contact angle of $\theta = 76^{\circ}$, salinity $S = 10$, and wall temperature $T_w = -5\text{ }^{\circ}\text{C}$ was selected as the reference value.

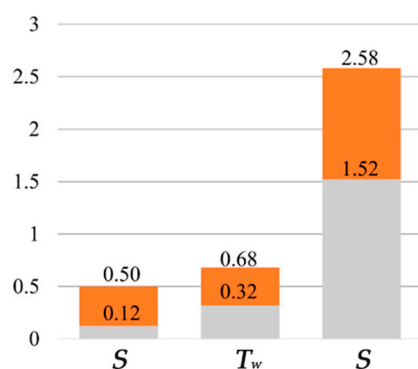


Figure 9. Sensitivity coefficients of different parameters.

It can be seen in the figure that the sensitivity coefficient of the salinity S varied from 0.12 to 0.50, the sensitivity coefficient of the wall temperature varied from 0.32 to 0.68, and the sensitivity coefficient of contact angle varied from 1.52 to 2.58. Compared to the salinity S and wall temperature T_w , the change in the contact angle θ had a sharper impact on the complete freezing time T_t , and increasing the contact angle more effectively prolonged the freezing time of the droplets.

5. Conclusions

A 2D axis-symmetric model combined with CLSVOF and the enthalpy–porosity method was proposed to predict the sessile seawater droplet freezing times on cold substrates. The initial profile of the sessile droplet was determined by the Young–Laplace equation. The freshwater and seawater droplet (salinity within 10‰ to 40‰) freezing on various substrates, with contact angles of 76° , 110° , and 150° and substrate temperatures of $-5\text{ }^{\circ}\text{C}$, $-10\text{ }^{\circ}\text{C}$, and $-15\text{ }^{\circ}\text{C}$, were described numerically. In addition, an experimental set-up with a camera recording the water–ice interface and a semiconductor refrigeration chip providing a cold substrate environment was established to validate the proposed numerical model. Good agreement was achieved by comparing the water–ice interface evolution between the numerically predicted and experimentally measured results.

The temperature distribution and freezing front development during a 10 μL sessile droplet freezing process were numerically investigated in detail. The freezing front increasing from the droplet bottom to the top was clearly shown. Due to the difference in the heat transfer coefficient between the liquid droplet and the surrounding air, the specific heat capacity and viscosity, and the existence of the solidification latent heat, the isotherms were non-uniform during the freezing process and formed a parabolic shape after completely freezing. The salinity, hydrophobic interaction, and substrate temperature significantly affected the freezing rates. This work provides new insights into the fundamentals of seawater freezing.

Author Contributions: Software, Y.Y.; Formal analysis, Y.W.; Investigation, Z.D.; Writing—original draft, Z.D.; Writing—review & editing, Z.D.; Funding acquisition, Z.W. All authors have read and agreed to the published version of the manuscript.

Funding: This research was funded by [the National Science and Technology Major Project] grant number [J2019-III-0017] and [the Fundamental Research Funds for the Central Universities] grant number [No. 3072022JC0302]. And The APC was funded by [Yanhua Wang].

Institutional Review Board Statement: Not applicable.

Informed Consent Statement: Not applicable.

Data Availability Statement: Not provided for privacy reasons.

Acknowledgments: This work was financially supported by the National Science and Technology Major Project, grant number J2019-III-0017 and the Fundamental Research Funds for the Central Universities, No. 3072022JC0302.

Conflicts of Interest: The authors declare no conflict of interest.

Nomenclature

| | |
|----------------|---|
| γ | Surface tension of liquid droplet |
| δ | Adhesion coefficient of liquid–solid surface |
| V | Droplet volume |
| θ | Contact angle of the surface |
| x, y, z | Cartesian coordinates |
| s | Contour line of droplet |
| A | Cross-sectional area of the droplet |
| b | Curvature of the curve at the initial point |
| g | Gravitational |
| T | Temperature |
| T_{liquid} | Average temperature of the liquid area |
| T_{solid} | Average temperature of the solid area |
| T_{sea} | Average temperature of the sea ice |
| $T_{freezing}$ | Freezing temperature |
| l_s | Thermal conductivity of sea ice |
| l_0 | Thermal conductivity of pure ice |
| T_w | Wall temperature |
| T_t | Time it takes for the droplets to freeze completely |
| S | Salinity |
| b | Scale coefficient |
| C_p | Specific heat capacity |
| L | Latent heat |
| \vec{u} | Velocity vector |
| Φ | Level-set function |
| ρ | Density |
| $\vec{\tau}$ | Stress tensor |
| \vec{F}_{sf} | Force arising from surface tension effects |

| | |
|----------------|--|
| S_y | Additional sink term induced by the solidification model |
| h | Sensible enthalpy |
| ΔH | Latent heat |
| H | Total enthalpy per control volume |
| E | Sensitivity coefficient |
| $\Delta A/A_0$ | Rate of change of the evaluation index |
| $\Delta B/B_0$ | Rate of change of the un-certainty factor |

References

- Dai, H.; Zhu, C.; Zhao, H.; Liu, S. A New Ice Accretion Model for Aircraft Icing Based on Phase-Field Method. *Appl. Sci.* **2021**, *11*, 5693. [[CrossRef](#)]
- Peng, S.; Hao, W.; Zhai, Y. Review of the research on icing mechanism of transmission lines and ice-melting technologies. In Proceedings of the 2015 5th International Conference on Electric Utility Deregulation and Restructuring and Power Technologies (DRPT), Changsha, China, 26–29 November 2015.
- Dalili, N.; Edrissy, A.; Carriveau, R. A review of surface engineering issues critical to wind turbine performance. *Renew. Sustain. Energy Rev.* **2009**, *13*, 428–438. [[CrossRef](#)]
- Meuler, A.J.; Smith, J.D.; Varanasi, K.K.; Mabry, J.M.; McKinley, G.H.; Cohen, R.E. Relationships between Water Wettability and Ice Adhesion. *ACS Appl. Mater. Interfaces* **2010**, *2*, 3100–3110. [[CrossRef](#)] [[PubMed](#)]
- Sanaye, S.; Shirazi, A. Four E analysis and multi-objective optimization of an ice thermal energy storage for air-conditioning applications. *Int. J. Refrig.* **2013**, *36*, 828–841. [[CrossRef](#)]
- Candanedo, J.A.; Dehkkordi, V.R.; Stylianou, M. Model-based predictive control of an ice storage device in a building cooling system. *Appl. Energy* **2013**, *111*, 1032–1045. [[CrossRef](#)]
- Clark, M.R.; Webb, J.; Kirk, P.J. Fine: Case analysis of a severe hailstorm using crowd sourced and conventional observations. *Meteorol. Appl.* **2017**, *25*, 472–492. [[CrossRef](#)]
- Kennedy, P.C.; Rutledge, S.A. Dual-Doppler and Multiparameter Radar Observations of a Bow-Echo Hailstorm. *Mon. Weather Rev.* **2009**, *123*, 921. [[CrossRef](#)]
- Punge, H.J.; Kunz, M. Hail observations and hailstorm characteristics in Europe: A review. *Atmos. Res.* **2016**, *176–177*, 159–184. [[CrossRef](#)]
- Vali, G. Repeatability and randomness in heterogeneous freezing nucleation. *Atmos. Chem. Phys. Discuss.* **2008**, *8*, 4059–4097. [[CrossRef](#)]
- Niedermeier, D.; Shaw, R.A.; Hartmann, S.; Wex, H.; Clauss, T.; Voigtländer, J.; Stratmann, F. Heterogeneous ice nucleation: Exploring the transition from stochastic to singular freezing behaviour. *Atmos. Chem. Phys.* **2011**, *11*, 8767–8775. [[CrossRef](#)]
- Kulinich, S.A.; Farzaneh, M. Ice adhesion on super-hydrophobic surfaces. *Appl. Surf. Sci.* **2009**, *255*, 8153–8157. [[CrossRef](#)]
- Zang, D.; Lin, K.; Wang, W.; Gu, Y.; Zhang, Y.; Geng, X.; Binks, B.P. Tunable shape transformation of freezing liquid water marbles. *Soft Matter* **2014**, *10*, 1309–1314. [[CrossRef](#)]
- Blake, J.; Thompson, D.; Raps, D.; Strobl, T. Simulating the freezing of supercooled water droplets impacting a cooled substrate. *AIAA J.* **2014**, *53*, 1725–1739. [[CrossRef](#)]
- Wang, Y.; Xue, J.; Wang, Q.; Chen, Q.; Ding, J. Verification of icephobic/anti-icing properties of a superhydrophobic surface. *ACS Appl. Mater. Interfaces* **2013**, *5*, 3370–3381. [[CrossRef](#)]
- Mishchenko, L.; Hatton, B.; Bahadur, V.; Taylor, J.A.; Krupenkin, T.; Aizenberg, J. Design of ice-free nanostructured surfaces based on repulsion of impacting water droplets. *ACS Nano* **2010**, *4*, 7699–7707. [[CrossRef](#)]
- Boinovich, L.; Emelyanenko, A.M.; Korolev, V.V.; Pashinin, A.S. Effect of wettability on sessile drop freezing: When superhydrophobicity stimulates an extreme freezing delay. *Langmuir* **2014**, *30*, 1659–1668. [[CrossRef](#)]
- Alizadeh, A.; Bahadur, V.; Zhong, S.; Shang, W.; Li, R.; Ruud, J.; Yamada, M.; Ge, L.; Dhinojwala, A.; Sohal, M. Temperature dependent droplet impact dynamics on flat and textured surfaces. *Appl. Phys. Lett.* **2012**, *100*, 111601. [[CrossRef](#)]
- Wilson, P.W.; Lu, W.; Xu, H.; Kim, P.; Kreder, M.J.; Alvarenga, J.; Aizenberg, J. Inhibition of ice nucleation by slippery liquid-infused porous surfaces (SLIPS). *Phys. Chem. Chem. Phys.* **2013**, *15*, 581–585. [[CrossRef](#)]
- Farhadi, S.; Farzaneh, M.; Kulinich, S.A. Anti-icing performance of superhydrophobic surfaces. *Appl. Surf. Sci.* **2011**, *257*, 6264–6269. [[CrossRef](#)]
- Hao, P.; Lv, C.; Zhang, X. Freezing of sessile water droplets on surfaces with various roughness and wettability. *Appl. Phys. Lett.* **2014**, *104*, 161609. [[CrossRef](#)]
- Han, S.W.; Jeong, J.; Lee, D.H. Ice-phobic behavior of superhydrophobic Al surface under various etching conditions. *J. Electroceram.* **2014**, *33*, 82–88. [[CrossRef](#)]
- Fang, G.; Amirfazli, A. Understanding the anti-icing behavior of superhydrophobic surfaces. *Surf. Innov.* **2014**, *2*, 94–102. [[CrossRef](#)]
- Li, K.; Xu, S.; Shi, W.; He, M.; Li, H.; Li, S.; Zhou, X.; Wang, J.; Song, Y. Investigating the effects of solid surfaces on ice nucleation. *Langmuir* **2012**, *28*, 10749–10754. [[CrossRef](#)]
- Jung, S.; Dorrestijn, M.; Raps, D.; Das, A.; Megaridis, C.M.; Poulikakos, D. Are superhydrophobic surfaces best for icephobicity? *Langmuir* **2011**, *27*, 3059–3066. [[CrossRef](#)] [[PubMed](#)]

26. Marin, A.G.; Enriquez, O.R.; Brunet, P.; Colinet, P.; Snoeijer, J.H. Universality of tip singularity formation in freezing water drops. *Phys. Rev. Lett.* **2014**, *113*, 054301. [[CrossRef](#)]
27. Ismail, M.F.; Waghmare, P.R. Universality in freezing of an asymmetric drop. *Appl. Phys. Lett.* **2016**, *109*, 234105. [[CrossRef](#)]
28. Shcherbina, A.Y.; Talley, L.D.; Rudnick, D.L. Direct observations of North Pacific ventilation: Brine rejection in the Okhotsk Sea. *Science* **2003**, *302*, 1952–1955. [[CrossRef](#)]
29. Boinovich, L.B.; Emelyanenko, A.M.; Emelyanenko, K.A.; Maslakov, K.I. Anti-icing properties of a superhydrophobic surface in a salt environment: An unexpected increase in freezing delay times for weak brine droplets. *Phys. Chem. Chem. Phys.* **2016**, *18*, 3131–3136. [[CrossRef](#)]
30. Strub, M.; Jabbour, O.; Strub, F.; Bédécarrats, J.P. Experimental study and modelling of the crystallization of a water droplet. *Int. J. Refrig.* **2003**, *26*, 59–68. [[CrossRef](#)]
31. Antonini, C.; Amirfazli, A.; Marengo, M. Drop impact and wettability: From hydrophilic to superhydrophobic surfaces. *Phys. Fluids* **2012**, *24*, 673–687. [[CrossRef](#)]
32. Alizadeh, A.; Yamada, M.; Li, R.; Shang, W.; Otta, S.; Zhong, S.; Ge, L.; Dhinojwala, A.; Conway, K.R.; Bahadur, V.; et al. Dynamics of Ice Nucleation on Water Repellent Surfaces. *Langmuir ACS J. Surf. Colloids* **2012**, *28*, 3180. [[CrossRef](#)]
33. Chaudhary, G.; Li, R. Freezing of water droplets on solid surfaces: An experimental and numerical study. *Exp. Therm. Fluid Sci.* **2014**, *57*, 86–93. [[CrossRef](#)]
34. Sun, J.; Gong, J.; Li, G. A lattice Boltzmann model for solidification of water droplet on cold flat plate. *Int. J. Refrig.* **2015**, *59*, 53–64. [[CrossRef](#)]
35. Liu, X.G.; Qu, Y.L.; Wang, Y.H.; Wang, M.; Wang, Z.Y.; Sun, H.O. Numerical analysis of two hollow drops simultaneously impacting a wet surface. *Phys. Fluids* **2021**, *33*, 43312. [[CrossRef](#)]
36. Liu, X.G.; Wang, Y.H.; Wang, Z.Y.; Sun, H.O.; Luan, Y.G. Numerical investigation of two hollow cylindrical droplets vertically impacting on dry flat surface simultaneously. *Phys. Fluids* **2020**, *32*, 113305. [[CrossRef](#)]
37. Zheng, Y.Z.; Li, Q.; Zheng, Z.H.; Zhu, J.F.; Cao, P.L. Modeling the impact, flattening and solidification of a molten droplet on a solid substrate during plasma spraying. *Appl. Surf. Sci.* **2014**, *317*, 526–533. [[CrossRef](#)]

Disclaimer/Publisher’s Note: The statements, opinions and data contained in all publications are solely those of the individual author(s) and contributor(s) and not of MDPI and/or the editor(s). MDPI and/or the editor(s) disclaim responsibility for any injury to people or property resulting from any ideas, methods, instructions or products referred to in the content.